University of Bristol - Explore Bristol Research
General rights

(iD) **G. Comandini,** (iD) **C. Khodr,** (iD) **V. P. Ting, et al.**

View Online   Export Citation   CrossMark

AIP
Publishing

Sound absorption in Hilbert fractal and coiled acoustic metamaterials

G. Comandini,[1,a] (ID) C. Khodr,[2,b] (ID) V. P. Ting,[1,c] (ID) M. Azarpeyvand,[3,d] (ID) and F. Scarpa[1,e] (ID)

AFFILIATIONS

[1]Bristol Composite Institute (BCI), School of Civil, Aerospace and Mechanical Engineering (CAME), University of Bristol, Bristol, United Kingdom
[2]Department of Mechanical Engineering, School of Civil, Aerospace and Mechanical Engineering (CAME), University of Bristol, Bristol, United Kingdom
[3]Department of Aerospace Engineering, School of Civil, Aerospace and Mechanical Engineering (CAME), University of Bristol, Bristol, United Kingdom

[a]Author to whom correspondence should be addressed: gianni.comandini@bristol.ac.uk
[b]Present address: Ecole Centrale de Lyon (ECL), Laboratoire de Mécanique des Fluides et Acoustique (LMFA), Écully, France.
Electronic mail: codor.khodr@ec-lyon.fr
[c]Electronic mail: v.ting@bristol.ac.uk
[d]Electronic mail: m.azarpeyvand@bristol.ac.uk
[e]Electronic mail: f.scarpa@bristol.ac.uk

ABSTRACT

We describe here a class of acoustic metamaterials with fractal Hilbert space-filling and coiled geometry with equal tortuosity for noise mitigation. Experiments are performed using a four-microphone impedance tube and benchmarked against non-viscous and viscothermal finite element models related to configurations spanning up to five fractal/geometry orders. We show that the acoustic absorption can be predicted by the resonance of the cavities associated with the tortuous paths. For a given fractal/geometry order, the acoustic absorption at specific frequencies is also enhanced by maximizing the difference between the minimum and maximum fluid particle velocity of the air inside the patterns. These principles can be used to design high-performance acoustic metamaterials for sound absorption over broad frequency ranges.

Rapid developments in the field of acoustic metamaterials have led to the design of new solutions for mitigating broadband noise.[1] Unlike classical absorbers, acoustic metamaterials rely on repeated/periodic sub-wavelength structures that modify the phase v_ϕ and group v_g velocities of sound.[2,3] It is now possible to design metamaterials with null or negative density ρ and bulk modulus κ,[4,5] and those anomalous properties are associated with wave phenomena, such as acoustic cloaking[6,7] ($\rho = 0$), super-lenses[8,9] (ρ, $\kappa < 0$), and sound slowness[10,11] ($\kappa = 0$). Labyrinth metamaterials have previously shown promising results for noise management applications.[12,13]

Fractal acoustic metamaterials are passive devices that can mitigate noise at particular frequencies.[14–21] Fractals are effective because of their order and geometrical characteristics, like the dimensions of internal slits.[22–24] However, as will be demonstrated, the acoustic metabehavior of the Hilbert fractal (HF) is not unique, and it can be related to non-fractal shapes with same lengths and gap widths. This

work demonstrates the existence of this similarity, in terms of resonance frequencies and root mean square (RMS) particle velocity fields inside the HF and coiled (non-fractal) families. The main objectives of this investigation are twofold: The first is about understanding the physical behavior of the fractal as an acoustic metamaterial; the second is to compare the response of the fractal metamaterial with a coiled geometry to observe the effect of the number of $\pi/2$ angles of the slits, which define the common topology of the Hilbert fractal and the coiled metamaterials.

Here, we describe the acoustic properties of 3D fractal-shaped metamaterials (MMs),[25,26] previously used only for applications involving the space-coiling of electromagnetic waves.[27,28] The description is made via impedance tube experiments and numerical simulations. The space-filling curve used in this work is the Hilbert fractal[29,30] [Figs. 1(f) and 1(g)]. The results are benchmarked against those from a non-fractal coiled geometry[31] [Fig. 1(h): second-order
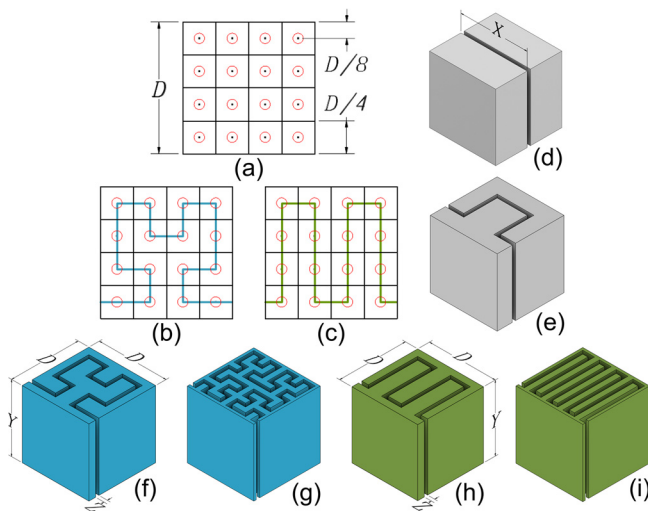
FIG. 1. (a) The common design process for the two metamaterials involves a subdivision of the square area into a grid with relative centers. Two distinctive connective paths of the central dots will create two different space filling curves, like the (b) Hilbert or (c) the coiled one. (f) Second-order Hilbert fractal. (h) Second-order coiled geometry. (d) and (e) Zero- and first-order geometries common for the two configurations; coiled and fractal. (g) Third-order Hilbert. (i) Third-order coiled geometry. The external dimension D is 50.8 mm, and Y and Z are the height and gap width.

coiled and Fig. 1(i): third-order coiled]. The patterns of the two configurations possess same lengths and internal volumes, with a minimum number of 90° angled paths for the coiled geometry [see Figs. 1(b) and 1(c), generated from the same area subdivision in Fig. 1(a) and supplementary material]. The fractal MMs are 3D-printed with polylactic acid (PLA) using an Ultimaker 2+ machine.[32] The percentage of the PLA infill during the printing was kept constant at 30%.

The Hilbert MM fractal patterns here range from the zeroth [Fig. 1(d)] to the fifth order, with gap widths [indicated as Z in Figs. 1(f) and 1(h)] between 0.5 and 3.0 mm. The maximum fractal order and gap dimensions are constrained by the manufacturing capability of the printer. Both Hilbert and coiled geometries with identical gap width and slit lengths ranging from the zeroth to the fifth order have been manufactured, tested, and simulated.

The acoustic absorption (AC) has been measured following the ASTM E2611-09 standard[33] by using a four-microphone impedance tube (more detail in the supplementary material). The frequency bandwidth considered here is within the 0.2–3 kHz range. Each measurement has been repeated ten times to remove outliers, using Chauvenet's criterion with normal distribution and 50% threshold.[34] We computed the resonance associated, using Eq. (1) with an equivalent rectangular section representing the labyrinth path with both ends open for each Hilbert fractal (from the zeroth order to the fifth order) and corresponding coiled geometry. In the equation, c is the airspeed of sound; i, j, and k are the vibrational mode numbers; and X is the fractal length [Fig. 1(d)] that is a function of the fractal order,

$$f = \frac{c}{2} \sqrt{\left(\frac{i^2}{X^2} + \frac{j^2}{Y^2} + \frac{k^2}{Z^2} \right)}. \tag{1}$$

Finite element (FE) simulations of the cavity modes with and without air viscosity have also been carried out using COMSOL Multiphysics. The analytical resonance frequencies are in good agreement with the ones simulated via FE (see Tables S1 and S2), with average differences ranging from 0.15% and 0.9% between the fifth and the first order. The acoustic absorption has also been simulated with full-scale FE models (more info on the FE in the supplementary material).

Figure 2 shows the direct comparison between the measured and simulated acoustic absorption of the fractal and coiled patterns at different orders. In Fig. 3, the absorption results show a resonance-type behavior, with peaks depending upon the order of the fractal or the coiled geometry. A broad agreement in terms of trends (but not necessarily values) can be observed between the numerical and experimental absorption coefficients. This is evident when observing the FE results in Figs. 2(a) and 2(d) and the experimental counterparts in Figs. 2(b), 2(c), 2(e), and 2(f). In Figs. 2(a) and 2(d), the absorption coefficient values found with the FE for the Hilbert and coiled geometries gave identical results; therefore, Figs. 2(a) and 2(d) show common curves between the Hilbert and the coiled configurations, since the results between the fractal and the coiled topologies overlap.

In the experimental results, the absorption coefficients in terms of trends tend to increase toward values of 0.5 at frequencies beyond 1.6 kHz. This behavior is remarkable, when one considers that these metamaterials have equivalent porosity between 2% and 63% only (see supplementary material). Some differences between the FEM [Figs. 2(a) and 2(d)] and experimental results [Figs. 2(b) and 2(e) for Hilbert and Figs. 2(c) and 2(f) for the coiled] are observed for the acoustic absorption related to zeroth, first, and second orders, as well as for the third, fourth, and fifth. Differences can be ascribed to manufacturing imperfections related to the test rig's fusion deposition molding and local slack. However, the viscous FE results mirror the periodic arrangement of the experimental absorption peaks; the experimental frequencies associated with the prominent peaks are more significant than the numerical ones (30% on average). The viscous FE tends to underestimate the amplitude of the AC peaks, although, at lower frequencies, the comparison is good (0.28 against 0.33 for the first peak of the second Hilbert fractal; see Fig. 3). The AC peaks correspond to fundamental cavity modes of the fractal pattern along the X direction, where $X = D(2^n)$ due to Helmholtz resonators effects (Fig. 3). In the equation, X represents the length of the fractal or coiled geometry [Fig. 1(d)], which is a function of the external dimensions of the cubic specimen D and the fractal order n. The variable n starts from the zeroth ($n = 0$) until the fifth order ($n = 5$). One can also observe the presence of small discrepancies between the resonances of the pattern cavities predicted by Eq. (1) and the non-viscous FE model (between 0.09% and 0.15%—see Tables S1 and S2). The frequencies corresponding to the absorption coefficient peaks in Figs. 2(a) and 2(d) are related to resonant phenomena inside the air ducts. Quite importantly, no difference of acoustic absorption is observed between the FE-simulated Hilbert and coiled patterns, no matter which fractal order is considered. This behavior is also substantially confirmed by the experiments, in terms of both AC peak frequencies and amplitudes [Figs. 2(b), 2(c), 2(e), and 2(f)]. The Hilbert fractal and the coiled geometry have a different number of 90° angles in their structures (Fig. S1 in the supplementary material) and consequently different internal numbers of right angles. It is, however, apparent that the absorption coefficient behavior globally depends on the overall path length and not on
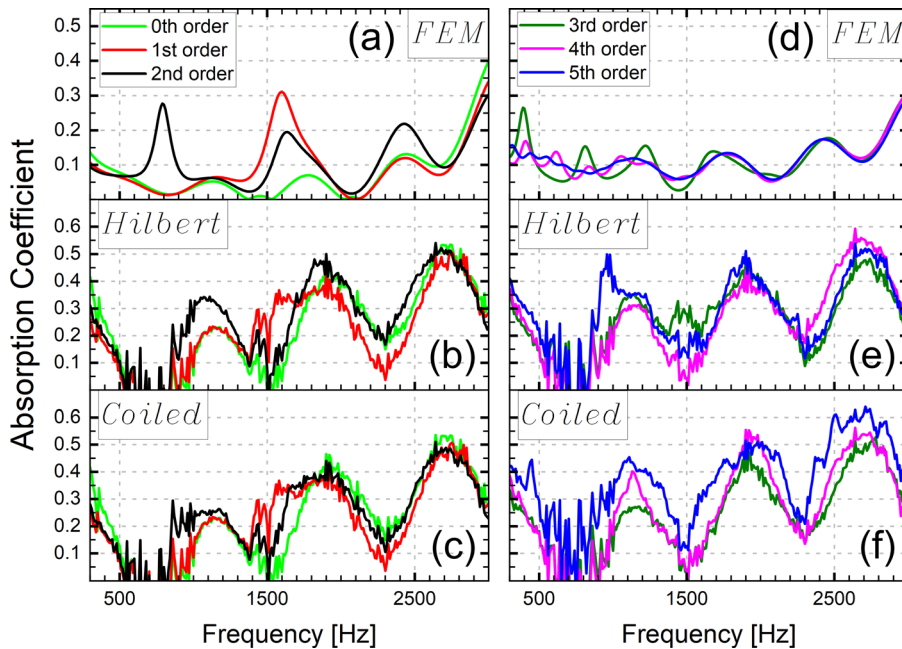
FIG. 2. Numerically modeled and experimentally measured absorption coefficients for the zeroth-, first-, and second-order Hilbert fractal and coiled geometries: (a) FE results for both configurations. Note that the results of numerical modeling for both geometries overlap; (b) experimental results using the Hilbert geometry; and (c) experimental results using the coiled geometry. Absorption coefficients for the third, fourth, and fifth orders of the two geometries: (d) FE model for both configurations; (e) experimental results using the Hilbert; and (f) experimental results using the coiled geometry.

the number of 90° angles forming the simple fractal/coiled polygonal chain.

The main outcome of the study is that the FE-simulated absorption coefficients of the Hilbert and coiled patterns coincide. The FE results (in particular, the viscothermal ones) underestimate the experimental ones but tend, however, to follow the experiments as a trend. On the other hand, the experimental absorption coefficients of the two

FIG. 3. Absorption coefficients for the second Hilbert and coiled patterns related to experiments, FE viscous and non-viscous models. Vertical lines are also drawn to indicate the first three resonance modes of the patterned cavities.

metamaterial configurations are similar (as predicted by the numerical results). This also confirms that the number of 90° angles has no significant role in the acoustic absorption performance.

Not all the acoustic cavity modes maximize the absorption [see, for example, the FE in Figs. 2(a) and 2(d), and Figs. S2 and S3]. To clarify this aspect, we have calculated the distribution of the RMS of the normalized local velocity inside the tortuous path of the two second-order metamaterials between 0.2 and 3 kHz [Fig. 4(b): second-order coiled and Fig. 4(d): second-order Hilbert]. To extract the RMS particle velocity inside the fractal and coiled geometries, a line corresponding to the midpoint of the 1 mm gap has been used. The segments forming the fractal/coiled geometry have been composed and presented in Figs. 4(a) and 4(c). The velocity has been normalized by dividing each RMS particle velocity field value with the velocity recorded at the inlet of the first-order Hilbert fractal {the latter coincides with the shape of the first-order coiled geometry [see Fig. 1(e)]}. The particle velocity field is calculated using a linearized Navier Stokes approach and thermo-viscous boundary layers within the gap. The maximum velocity values generally occur at the inlet and outlet of the metamaterial. The discontinuities observed in Figs. 4(a) and 4(c) are due to the sharp changes in velocity at the beginning and end of each segment forming the polygonal path. The minimum always occurs in the central area of the pattern.

The number of maximum or minimum values of the velocity field is linked to the vibrational mode in correspondence of the AC peaks. For instance, for the first vibrational mode of the second-order Hilbert fractal [Fig. 4(d)] and coiled geometry [Fig. 4(b)] at 792 Hz, the maximum values are at the inlet [segment I for Figs. 4(a) and 4(c)] and outlet [segment IX for Fig. 4(a) and XIII for Fig. 4(c)]. The only minimum (at 792 Hz) is in the central part [at segment V in Fig. 4(a), and VII in Fig. 4(c)]. Three maximum values are present for the second vibrational mode at 1633 Hz, with two minima in the central part.
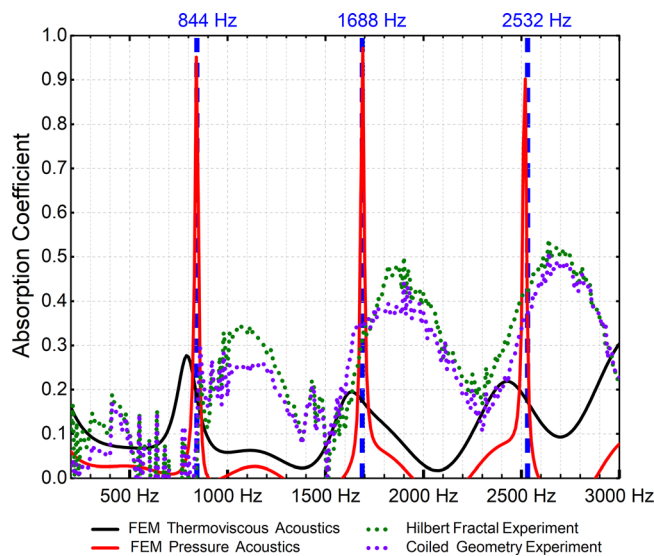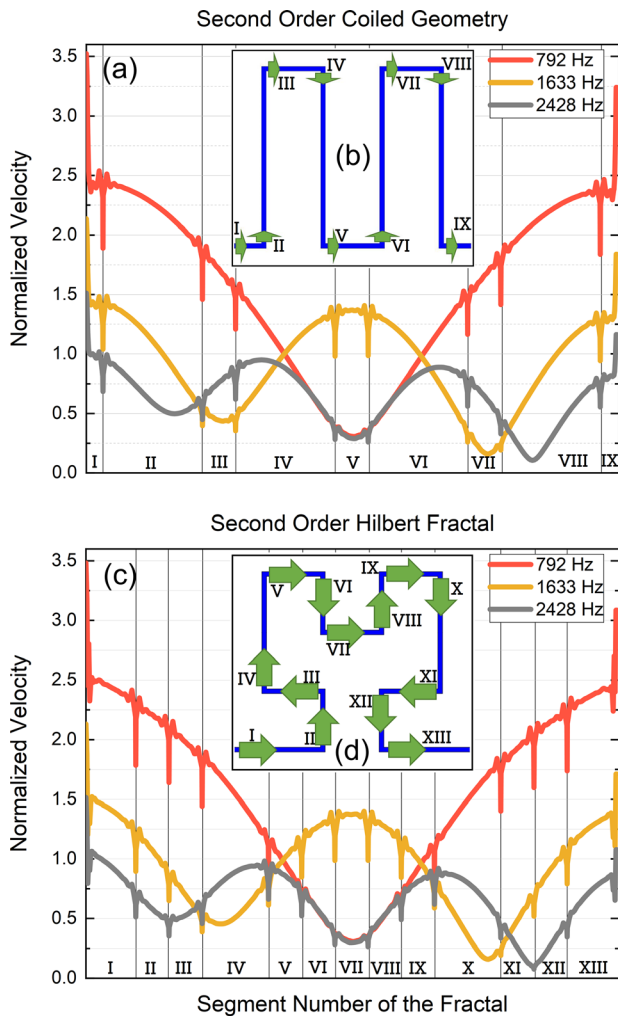
FIG. 4. (a) Calculated distribution of the RMS viscous FE velocity inside the second-order coiled geometry, normalized with the RMS value of the velocity at the inlet of the first-order Hilbert fractal (5.6 mm/s) that coincide as geometry to the first-order coiled. The velocity graph refers to AC peaks in [Fig. 1(h)] at 792, 1633, and 2428 Hz. Drops in velocity coincide with losses due at the 90° angles of the patterns. (b) Locations and directions of the velocity field. Every roman numeral identifies a segment of the geometry where the velocity has been calculated. (c) RMS local velocity field corresponding to the three AC peaks for the second Hilbert fractal between 200 and 3000 Hz [Fig. 1(f)]. (d) Position and direction of the calculated velocity field in the Hilbert fractal, second order.

For the last vibrational mode reported here in Fig. 4, the number of max peaks at 2428 Hz is four, and the minimum values are three. As a general behavior, we can state that the distance among the maximum and minimum values decreases with the order of the vibrational mode. Also, the number of peaks increases with the increase in the vibrational mode, but to a lesser extent compared to the RMS particle velocity field. This phenomenon can be observed by looking at the AC peak at 792 Hz of the second-order Hilbert fractal [Fig. 4(c)], which coincides with the maximum difference between the min and max normalized velocity at the middle of the tortuous path [segment VII,

relative to Fig. 4(d)]. At the other frequencies corresponding to the absorption coefficient FE peaks (1633 and 2428 Hz), the velocity field shows the presence of two and three minima with lower maximum difference (0.8 and 0.5). A very similar behavior is observed for the coiled pattern with the same order [Fig. 4(a)]. The number of right angles forming the two polygonal geometries is different, but the normalized velocity field is similar for the two geometries [Figs. 4(a) and 4(c)]. Another noticeable point is that the behavior of the absorption coefficient peaks and the maximum difference of internal velocities follow the fractal orders of the geometries, in terms of number of peaks and valleys. The maximum difference between the lower and higher values of the RMS velocity only occur in correspondence of the main absorption coefficient peaks, and this is common to the two geometries.

Fractal acoustic metamaterials can be effectively used to tailor the acoustic absorption over a broad frequency range by designing the pattern with specific tortuous path lengths and depth of the slit. The absorption is provided through a series of multiple peaks that depend on the fractal or geometric order of the patterns. The frequencies corresponding to those peaks can be predicted quite well by the resonances of non-viscous fluid cavities with overall equal path length and depth of the patterns. Finite elements that include viscothermal effects simulate peaks corresponding to slightly lower frequencies and trends in broad agreement with experimental data, although the latter show higher absorption coefficient values. For a given fractal/geometry order, the maximum values of the absorption correspond to particle air velocity fields inside the tortuous paths that feature the largest difference between minimum and maximum velocity values. No substantial difference in absorption coefficient behavior is observed between the fractal Hilbert and the coiled geometry: although with different 90° values, the two configurations have the same tortuosity X/D. The fact that the number of 90° angles inside a polygonal path does not influence significantly the results is important. However, we cannot state that the acoustic output is invariant, whichever angle of the topology is used to create the fractal. We do not consider here angles with values above or below $\pi/2$. A key conclusion to understand the physics of the acoustics in these fractal metamaterials is that the internal path lengths and gap widths are critical and provide the equivalence between the coiled and Hilbert fractal geometries. The fractal Hilbert geometry is, however, a self-filling space by definition: This pattern can, therefore, be a preferred choice to design space-optimized fractal geometries to enhance the acoustic behavior via metamaterials.

See the supplementary material that contains descriptions of the materials used for the 3D printing, measurement apparatus and technique, and finite element models. Added information is related to tables containing the theoretical values of the cavity resonances, distributions of porosity, and comparisons between the locations of the FE acoustic absorption peaks with the corresponding theoretical values.

AUTHOR DECLARATIONS

Conflict of Interest

The authors declare no conflict of interests exist for the development of this work.

DATA AVAILABILITY

The data that support the findings of this study are available within the article and its supplementary material.

REFERENCES

[1]X. Fang, J. Wen, B. Bonello, J. Yin, and D. Yu, "Ultra-low and ultra-broadband nonlinear acoustic metamaterials," Nat. Commun. **8**, 1288 (2017).

[2]N. Jiménez, W. Huang, V. Romero-García, V. Pagneux, and J.-P. Groby, "Ultra-thin metamaterial for perfect and quasi-omnidirectional sound absorption," Appl. Phys. Lett. **109**, 121902 (2016).

[3]X.-J. Li, C. Xue, L. Fan, S.-Y. Zhang, Z. Chen, J. Ding, and H. Zhang, "Simultaneous realization of negative group velocity, fast and slow acoustic waves in a metamaterial," Appl. Phys. Lett. **108**, 231904 (2016).

[4]R. Graciá-Salgado, V. M. García-Chocano, D. Torrent, and J. Sánchez-Dehesa, "Negative mass density and ρ-near-zero quasi-two-dimensional metamaterials: Design and applications," Phys. Rev. B **88**, 224305 (2013).

[5]S. A. Cummer, J. Christensen, and A. Alù, "Controlling sound with acoustic metamaterials," Nat. Rev. Mater. **1**, 16001 (2016).

[6]S.-W. Fan, S.-D. Zhao, L. Cao, Y. Zhu, A.-L. Chen, Y.-F. Wang, K. Donda, Y.-S. Wang, and B. Assouar, "Reconfigurable curved metasurface for acoustic cloaking and illusion," Phys. Rev. B **101**, 024104 (2020).

[7]Z. Basiri, M. H. Fakheri, A. Abdolali, and C. Shen, "Non-closed acoustic cloaking devices enabled by sequential-step linear coordinate transformations," Sci. Rep. **11**, 1845 (2021).

[8]J. J. Park, C. M. Park, K. Lee, and S. H. Lee, "Acoustic superlens using membrane-based metamaterials," Appl. Phys. Lett. **106**, 051901 (2015).

[9]A. K. Iyer and G. V. Eleftheriades, "Mechanisms of subdiffraction free-space imaging using a transmission-line metamaterial superlens: An experimental verification," Appl. Phys. Lett. **92**, 131105 (2008).

[10]Y. Li, B. Liang, Z.-M. Gu, X.-Y. Zou, and J.-C. Cheng, "Unidirectional acoustic transmission through a prism with near-zero refractive index," Appl. Phys. Lett. **103**, 053505 (2013).

[11]P. S. Ma, H. J. Lee, and Y. Y. Kim, "Dispersion suppression of guided elastic waves by anisotropic metamaterial," J. Acoust. Soc. Am. **138**, EL77–EL82 (2015).

[12]Y. Xie, A. Konneker, B.-I. Popa, and S. A. Cummer, "Tapered labyrinthine acoustic metamaterials for broadband impedance matching," Appl. Phys. Lett. **103**, 201906 (2013).

[13]S. Kumar and H. P. Lee, "Labyrinthine acoustic metastructures enabling broadband sound absorption and ventilation," Appl. Phys. Lett. **116**, 134103 (2020).

[14]Q. J. Lim, P. Wang, S. J. A. Koh, E. H. Khoo, and K. Bertoldi, "Wave propagation in fractal-inspired self-similar beam lattices," Appl. Phys. Lett. **107**, 221911 (2015).

[15]A. Krushynska, F. Bosia, and N. M. Pugno, "Fractal and bio-inspired labyrinthine acoustic metamaterials," J. Acoust. Soc. Am. **143**, 1714–1714 (2018).

[16]J. Liu, L. Li, B. Xia, and X. Man, "Fractal labyrinthine acoustic metamaterial in planar lattices," Int. J. Solids Struct. **132–133**, 20–30 (2018).

[17]B. Xia, L. Li, J. Liu, and D. Yu, "Acoustic metamaterial with fractal coiling up space for sound blocking in a deep subwavelength scale," J. Vib. Acoust. **140**, 011011 (2018).

[18]P. Zhao, K. Zhang, and Z. Deng, "Elastic wave propagation in lattice metamaterials with koch fractal," Acta Mech. Solida Sin. **33**, 600–611 (2020).

[19]X. Zhao, G. Liu, and D. Xia, "Maze-like acoustic metamaterial for low-frequency broadband noise suppression," Appl. Phys. Express **13**, 027002 (2020).

[20]G. Wu, Y. Ke, L. Zhang, and M. Tao, "Acoustic manipulation of fractal metamaterials with negative properties and near-zero densities," Appl. Phys. Express **15**, 014002 (2022).

[21]F. Morandi, M. Miniaci, A. Marzani, L. Barbaresi, and M. Garai, "Standardised acoustic characterisation of sonic crystals noise barriers: Sound insulation and reflection properties," Appl. Acoust. **114**, 294–306 (2016).

[22]X. Man, T. Liu, B. Xia, Z. Luo, L. Xie, and J. Liu, "Space-coiling fractal metamaterial with multi-bandgaps on subwavelength scale," J. Sound Vib. **423**, 322–339 (2018).

[23]L. Xiang, G. Wang, and C. Zhu, "Controlling sound transmission by space-coiling fractal acoustic metamaterials with broadband on the subwavelength scale," Appl. Acoust. **188**, 108585 (2022).

[24]X. Man, Z. Luo, J. Liu, and B. Xia, "Hilbert fractal acoustic metamaterials with negative mass density and bulk modulus on subwavelength scale," Mater. Des. **180**, 107911 (2019).

[25]G. Y. Song, Q. Cheng, B. Huang, H. Y. Dong, and T. J. Cui, "Broadband fractal acoustic metamaterials for low-frequency sound attenuation," Appl. Phys. Lett. **109**, 131901 (2016).

[26]I. Grigorenko, "Nanostructures with the hilbert curve geometry as surface enhanced raman scattering substrates," Appl. Phys. Lett. **103**, 043123 (2013).

[27]Y. Xie, S. Ye, C. Reyes, P. Sithikong, B.-I. Popa, B. J. Wiley, and S. A. Cummer, "Microwave metamaterials made by fused deposition 3D printing of a highly conductive copper-based filament," Appl. Phys. Lett. **110**, 181903 (2017).

[28]B. Wang, K. H. Teo, T. Nishino, W. Yerazunis, J. Barnwell, and J. Zhang, "Experiments on wireless power transfer with metamaterials," Appl. Phys. Lett. **98**, 254101 (2011).

[29]X. Zhao, G. Liu, C. Zhang, D. Xia, and Z. Lu, "Fractal acoustic metamaterials for transformer noise reduction," Appl. Phys. Lett. **113**, 074101 (2018).

[30]X.-F. Man, B.-Z. Xia, Z. Luo, and J. Liu, "3D hilbert fractal acoustic metamaterials: Low-frequency and multi-band sound insulation," J. Phys. D: Appl. Phys. **52**, 195302 (2019).

[31]J. K. Lawder, "The application of space-filling curves to the storage and retrieval of multi-dimensional data," Ph.D. thesis (Citeseer, 2000).

[32]D. D. Hernandez, "Factors affecting dimensional precision of consumer 3d printing," Int. J. Aviat. Aeronaut. Aerosp. **2**, 2 (2015).

[33]ASTM International, *ASTM E2611-09 Standard Test Method for Measurement of Normal Incidence Sound Transmission of Acoustical Materials Based on the Transfer Matrix Method* (ASTM, 2009).

[34]L. Lin and P. D. Sherman, "Cleaning data the Chauvenet way," in The Proceedings of the SouthEast SAS Users Group, SESUG Proceedings, Paper SA11 (2007).